Optimum Corner Reflectors for Calibration of Imaging Radars

Kamal Sarabandi, *Senior Member, IEEE*, and Tsen-Chieh Chiu

Abstract—**Trihedral corner reflectors are widely used as calibration targets or imaging radars because of their large radar cross section (RCS) and extremely wide RCS pattern. An important source of uncertainty in the RCS of trihedral sitting on a ground plane is the coherent interaction of the ground plane with the trihedral. At UHF and low microwave frequencies the large physical size of corner reflectors become a limiting factor in regard to difficulties in field deployment and deviation of their RCS from the expected values. In this paper, a general class of corner reflectors with high-aperture efficiency referred to as self-illuminating corner reflectors, is introduced whose coherent interaction with their surrounding terrain is minimized and their total surface area is two-thirds of that of a triangular corner reflector having the same maximum RCS. Analytical expressions based on geometrical optics and a new numerical solution based on near-field physical optics for the RCS of two simple self-illuminating corner reflectors are presented and compared with backscatter measurements. Also the panel geometry for an optimum corner reflector which has the shortest edge length among polygonal self-illuminating corner reflectors is obtained. High-aperture efficiency is achieved at the expense of azimuth and elevation beamwidth. It is shown that the 1-dB RCS beamwidths of the optimal corner reflectors, both in azimuth and elevation directions, are about 16°, which is sufficient for most practical applications. RCS measurements of corner reflectors in the presence of a ground plane show that the RCS of self-illuminating corner reflectors are less affected by the coherent ground interaction.**

I. Introduction

QUANTITATIVE interpretation of images acquired by synthetic aperture radars requires an external calibration procedure. Generally, in calibration procedures the radar return from individual pixels in the image is compared with that of a pixel including the calibration target with known scattering matrix [1], [2]. The success of an external calibration procedure is directly influenced by five counteracting characteristics of the calibration target. These include 1) large radar cross section (RCS), 2) wide RCS pattern, 3) small physical size, 4) stable RCS, and 5) insensitive RCS to the surrounding environment. Noting that the calibration targets are deployed over a surface with nonzero radar backscatter, it is required that the RCS of the target are much larger than the direct backscatter of the terrain and also the coherent interaction of the target and the terrain be as small as possible. The wide RCS pattern or insensitivity of target alignment to the radar coordinate and the small physical size requirements are needed to assure the ease of target deployment under the field conditions.

Trihedral corner reflectors have long been used as radar reflectors and calibration targets [3]. With the advances in the imaging radar technology and the need for quantitative data, trihedral corner reflectors, having most of the above mentioned characteristics, are being widely used as a calibration target for imaging radars [2], [7]. However, at low frequencies such as P and L band the physical size of the panels for the required RCS becomes prohibitively large. In these cases, the trihedral structure is susceptible to geometrical deformation which would cause a departure from the theoretical RCS of the target. In a recent cross-calibration study using the JPL AIRSAR and the University of Michigan, Ann Arbor, polarimetric scatterometers it was shown that the coherent and incoherent interaction of the ground surface with a trihedral corner reflector can distort the expected scattering matrix of the target significantly [8]. The uncertainties in the RCS and the scattering matrix of the trihedrals exceed the maximum tolerable errors required for most remote sensing applications.

Traditionally, the choice of panel geometry for corner reflectors as been a triangular shape due, perhaps, to the simplicity in the structural design and manufacturing. In this paper, an optimum panel geometry or a corner reflector sought so that the RCS of the reflector is least affected by the coherent ground interaction and its RCS is maximized for a given panel area while minimizing the edge length. As will be shown later, the first two conditions are met if the panels of the corner reflector are completely illuminated after two reflections of the incoming wave from the other panels. A general procedure for characterizing the panel geometry of a self-illuminating corner reflector is outlined and it is shown that the surface area of such corner reflector is 2/3 of the surface area of a trihedral corner reflector having identical RCS at boresight illumination. Then the geometry of an optimum reflector which has the shortest edge length among the self-illuminating polygonal corner reflectors is obtained. Two simple self-illuminating reflectors, namely, the square and pentagonal corner reflectors are considered in this paper. Analytical solutions for backscatter cross section of these corner reflectors are derived and compared with the backscatter measurements. In what follows, first the theoretical analyses for the radar cross section based on the geometrical optics (GO) and near-field physical optics (PO) approximation are given, then experimental results for a pentagonal corner reflector and a square corner reflector at X-band are presented and compared with those obtained from their triangular corner-reflector counterpart. Also the measured backscatter from the

Manuscript received April 27, 1995; revised February 9, 1996. This work was supported by the Jet Propulsion Laboratory, California Institute of Technology, under Contract JPL 958749.

The authors are with the Department of Electrical Engineering and Computer Science, The University of Michigan, Ann Arbor, MI 48109 USA.

Publisher Item Identifier S 0018-926X(96)07545-X.

pentagonal and triangular corner reflectors in the presence of a smooth perfectly conducting and lossy dielectric ground planes are presented. It is also shown that the scattering matrix and the RCS of self-illuminating corner reflectors are less affected by the ground plane.

II. Theoretical Analysis

A. RCS Calculation

In this section, a brief discussion on the evaluation of RCS for corner reflector with arbitrary panel geometry based on the GO and a near-field PO approximations is given. Here, the region of interest for calculation of RCS is confined to the first quadrant containing the corner reflector's boresight. The literature concerning calculation of RCS pattern of corner reflectors is limited to the GO solution or triangular and square corner reflectors over a limited region around their boresight [3]–[5]. The GO solution for RCS pattern of square corner reflectors is reported incorrectly [4]. Analytical expression for the RCS pattern of triangular, square, and pentagonal corner reflectors based on GO approximation are derived in this section. These results are valid over a wide range of incidence angles. More accurate approximate solutions such as geometrical theory of diffraction (GTD), uniform theory of diffraction (UTD), or physical theory of diffraction (PTD) have been applied to dihedral corner reflectors [9], [12]. Although the application of UTD or PTD to simple geometries is rather simple, for concave scatterers such as trihedral corner reflectors the analysis becomes very complex. The difficulty is in the computation of the diffracted wave contributions that enter the corner reflector cavity. Besides, for the problem at hand where the RCS is required only around the boresight, and the dimensions of the panels are much larger than the wavelength, the contribution from the edge diffraction can be ignored. It should also be noted that exact numerical solutions, such as the finite element and the method of moments, for most practical corner reflectors (typical dimension $>10\lambda$) are not tractable.

Considering a right-angle corner reflector it can easily be shown that for any incident ray entering the corner reflector cavity, after triple reflection there exists a specular point in the backscatter direction and, therefore, the GO solution can be used for the RCS calculations. To outline a procedure for the RCS calculation using the GO method, consider a corner reflector with arbitrary panel geometry whose internal edges form the axes of a Cartesian coordinate system (x, y, z), as shown in Fig. 1(a). Let us denote the panels in x–y, y–z, and z–x planes, respectively, by panel #1, #2, and #3. To compute the backscatter contribution from each panel, the illuminated area on each panel must be calculated. Panel #1 is illuminated by two plane waves resulting from double reflections of the incident wave from 1) panel #2, then panel #3 and 2) panel #3, then panel #2. The propagation unit vector of the image of the incident wave in panel #2 and its image in panel #3 are, respectively, given by

$$\hat{k}_{i2} = \hat{k}_i - 2(\hat{x} \cdot \hat{k}_i)\hat{x},$$
$$\hat{k}_{i23} = -\hat{k}_i + 2(\hat{z} \cdot \hat{k}_i)\hat{z}$$

where

$$\hat{k}_i = -\sin\theta\cos\phi\hat{x} - \sin\theta\sin\phi\hat{y} - \cos\theta\hat{z}.$$

If panels #2 and #3 were infinite in extent, panel #1 would entirely be illuminated. However, both panel #2 and panel #3 are finite and, therefore, only a portion of panel #1 is illuminated. In this case, panel #2 can be viewed as window for the image wave $\hat{k}_{i2}$ which partially illuminates panel #3, as shown in Fig. 1(b) (indicated by S_{23}). Similarly, the area S_{23} on panel #3 an be regarded as a window for the image wave $\hat{k}_{i23}$ that partially illuminates panel #1. The area of this region is denoted by A_1^{23}. In a similar manner, the illuminated area on panel #1 by the second image wave $\hat{k}_{i32}$) an be obtained and is denoted by A_1^{32}. It should be noted that these illuminated areas on x–y plane may exceed the geometrical extent of panel #1. In such cases, A_1^{23} and A_1^{32} are the areas of the intersection of the illuminated regions and panel #1. The two image waves that illuminate panel #1 are parallel ($\hat{k}_{i23} = \hat{k}_{i32}$), in-phase, and copolarized. The expression representing the image wave is found to be

$$\boldsymbol{E}_{im} = [-\boldsymbol{E}_0 + 2(\hat{z} \cdot \boldsymbol{E}_0)\hat{z}]e^{ik_0\hat{k}_{i23}\cdot\boldsymbol{r}}$$

which can be used to find the backscatter from panel #1. The following expression for the scattered field from panel #1 can be obtained [10]

$$\boldsymbol{E}_{s1} = \frac{iA_1}{\lambda_0}\cos\theta\boldsymbol{E}_0 \tag{1}$$

where $A_1 = A_1^{23} + A_1^{32}$. This process must be repeated to find the backscatter contribution of panel #2 ($\boldsymbol{E}_{s2}$) and panel #3 ($\boldsymbol{E}_{s3}$) from which the overall RCS can be computed from begin

$$\sigma = 4\pi\left|\sum_{j=1}^{3}\boldsymbol{E}_{sj}\right|^2. \tag{2}$$

The GO solution for estimation of the RCS is simple and widely used, but its accuracy degrades when a typical dimension of the scatterer becomes comparable with the wavelength. A more accurate estimation of RCS can be obtained using the PO solution. The PO solution for flat plates cannot be used directly for corner reflectors. The difficulty is in the calculation of the PO currents generated by the reflected fields. Basically, the panels are in the near-field region of each other and the reflected fields can no longer be assumed to be plane waves. In this case, the PO current in panel #2 induced by the primary PO current on panel #1 ($\boldsymbol{J}_1$) must be computed from

$$\boldsymbol{J}_{12} = 2\hat{x} \times \boldsymbol{H}_{12}^s$$

where

$$\boldsymbol{H}_{12}^s = \int \boldsymbol{J}_1(\boldsymbol{r}')\nabla \times \overline{\overline{\boldsymbol{G}}}(\boldsymbol{r}, \boldsymbol{r}')\,d\boldsymbol{r}'. \tag{3}$$

Noting that [13]

$$\nabla \times \overline{\overline{\boldsymbol{G}}}(\boldsymbol{r}, r') = \left(ik_0 - \frac{1}{|\boldsymbol{r}-\boldsymbol{r}'|}\right)\frac{e^{ik_0|\boldsymbol{r}-\boldsymbol{r}'|}}{4\pi|\boldsymbol{r}-\boldsymbol{r}'|^2}(\boldsymbol{r}-\boldsymbol{r}') \times \overline{\overline{\boldsymbol{I}}}$$

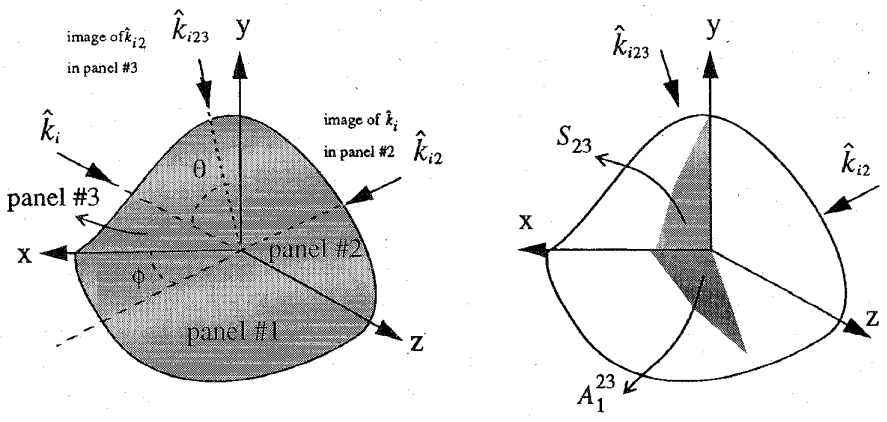

(a) (b)

Fig. 1. (a) A corner reflector with arbitrary panel geometry illuminated by a plane wave. (b) The lit area on panel #1 after two reflections of the incident wave from panel #2 and then panel #1.

(3) can be reduced to

$$\boldsymbol{H}_{12}^{s} = \int (\boldsymbol{r}-\boldsymbol{r}') \times \boldsymbol{J}_1(\boldsymbol{r}') \left(ik_0 - \frac{1}{|\boldsymbol{r}-\boldsymbol{r}'|} \right) \frac{e^{ik_0|\boldsymbol{r}-\boldsymbol{r}'|}}{4\pi|\boldsymbol{r}-\boldsymbol{r}'|^2}\, d\boldsymbol{r}'. \tag{4}$$

Finally, to find the induced current on panel #3 ($\boldsymbol{J}_{123}$), $\boldsymbol{J}_{12}$ must be used in an integral similar to (4). Unfortunately, closed-form expression for (4) cannot be obtained, and costly numerical integrations must be performed. Basically, to find the scattered field, a six-folded integration is required which makes the RCS evaluation numerically very inefficient. To make the RCS evaluation more efficient without compromising the accuracy too much, a hybrid GO–PO solution is considered [9]. In this approach, for the first reflection, the GO solution and/or the two following reflections the PO solution are used. This method will be referred to as the GO–PO–PO solution. The GO–PO–PO solution requires four-folded numerical integration, and its validity can be justified by noting that the majority of the reflection points on the third panel are far enough from the reflection points on the first panel; thus, the GO solution can be used for the first reflection. It should be mentioned here that the RCS calculations for corner reflectors based on a GO–GO–PO method is not, in any significant way, different from the GO solution and, therefore, it is not pursued in this paper.

B. Triangular Corner Reflector

The radar cross section of triangular corner reflectors has been characterized and studied thoroughly [4], [6], [11]. Backscatter RCS measurements indicate that the GO solution can accurately predict the RCS of triangular corner reflectors near boresight. An approximate expression for the backscatter RCS of triangular corner reflectors based on GO solution is given by [4]

$$\sigma(\theta,\phi) \approx \frac{4\pi}{\lambda^2} \cdot l^4 \cdot \{\cos\theta + \sin\theta(\sin\phi + \cos\phi) - 2 \cdot [\cos\theta + \sin\theta(\sin\phi + \cos\phi)]^{-1}\}^2 \tag{5}$$

where l is the trihedral height, as shown in Fig. 3. This approximation is valid when $l \gg \lambda$ and θ and ϕ are near boresight. A more accurate GO solution which is valid over a wide range of θ and ϕ is given in Appendix A. To examine whether the GO–PO–PO method produces a more accurate RCS estimation or not, the RCS pattern of a triangular corner reflector with $l = 10\lambda$ at 9.5 GHz was measured and compared with the GO and GO–PO–PO solutions. Fig. 2(a) and (b) shows the horizontal and elevation RCS patterns of the trihedral as measured by a polarimetric radar and predicted by the GO and GO–PO–PO methods. It should be noted that the elevation pattern is defined as the $\phi = 45°$ plane and the elevation angle is $54.73° - \theta$. In practice, the elevation pattern can be measured easily. However, this is not the case for the azimuth pattern where $\theta = 54.73°$ must be kept constant (conical surface). Instead, the pattern in the horizontal plane is measured. The horizontal plane is defined as the plane which contains the trihedral boresight and is parallel to the lower panel edge. If the incident direction in the horizontal plane as measured from the boresight direction is denoted by α, then

$$\phi = \tan^{-1}\left[\frac{\sqrt{2}\cos\alpha + \sqrt{3}\sin\alpha}{\sqrt{2}\cos\alpha - \sqrt{3}\sin\alpha}\right],$$
$$\theta = \cos^{-1}\left[\frac{\cos\alpha}{\sqrt{3}}\right].$$

Fig. 2(a) and (b) shows that the GO and GO–PO–PO solutions agree very well with the measured data and, hence, the GO solution is accurate enough in this case. The small ripple in the measured data is caused by the direct backscatter contribution of single and double bounce reflections which are not included in our GO and GO–PO–PO solutions.

C. Pentagonal and Square-Corner Reflectors

For a triangular corner reflector at boresight incidence, only a portion of each panel is illuminated, as shown in Fig. 3(a). Appendix A gives the expressions for the area of the lit regions as a function of incidence angle for a triangular corner reflector. In characterization of the lit regions or a triangular corner reflector, it is noticed that at boresight incidence $\phi = 45°$, $\theta = 54.7°$ where the RCS is maximized

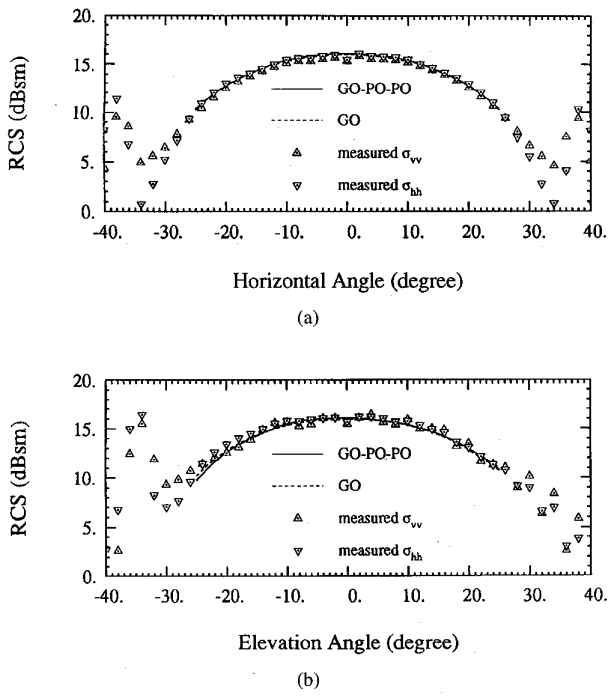

Fig. 2. RCS patterns of a triangular corner reflector as function of (a) horizontal and (b) elevation angles. $l = 10\lambda$ at 9.5 GHz.

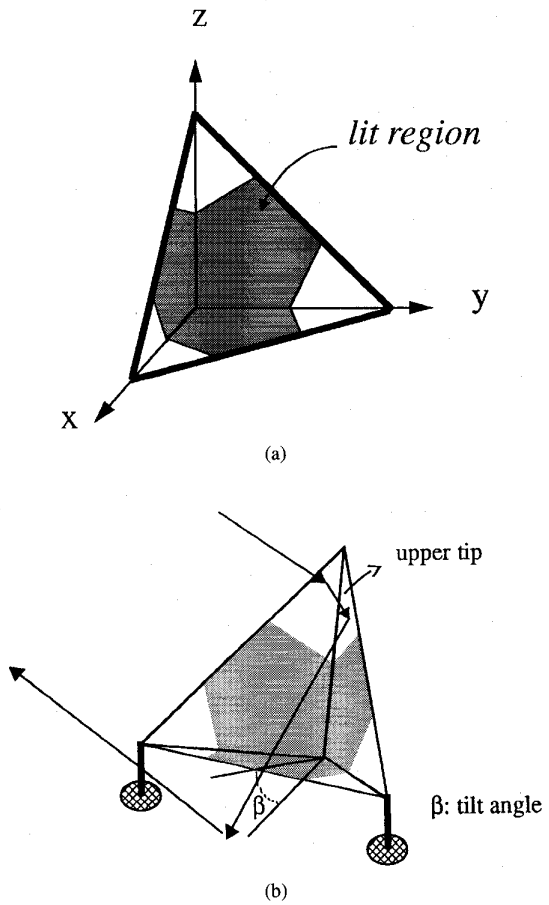

Fig. 3. (a) The geometry of lit region on a triangular corner reflector. (b) The interaction of a triangular corner reflector with the round plane.

only two-thirds of the area on each panel is lit and gives rise to the maximum RCS ($\sigma = 4\pi l^4/3\lambda^2$). The geometry of the lit area in each panel is a pentagon, as shown in Fig. 3. This fact has been known for a long time [11], [12], but no formal analysis or discussion on the performance of a corner reflector with pentagonal panel geometry can be found. One obvious advantage of a corner reflector with pentagonal panels which will be referred to as a pentagonal corner reflector, is the reduction in the surface area (weight) by 1/3 without reducing the maximum RCS. An important feature of corner reflector when considered as a calibration target for imaging radars is its interaction with the ground plane. Since the reflected rays from the tips of the trihedral corner reflectors are not captured by the other panels, they may interact with the scatterers on the ground plane and give rise to some unknown backscatter contribution [see Fig. 3(b)]. For high angles of incidence where the lower panel is almost parallel with the ground plane the specular reflection from the ground plane illuminates the upper tip of the corner reflector which, again, can increase its RCS. For the pentagonal corner reflector, on the other hand, all the rays that enter the reflector's cavity experience the triple reflection and return to the radar. Therefore, its interaction with the ground plane is expected to be minimal. It can be shown that a corner reflector with square-panel geometry has the same property (self-illuminating).

The RCS pattern for these reflectors can be obtained using the GO method in a rather straightforward manner. Analytical expressions for the RCS of the square and pentagonal corner reflectors are given in Appendixes B and C, respectively. Although square corner reflectors have long been used, their maximum RCS and their RCS patterns have been reported incorrectly. For example, the expression for the RCS pattern reported by Ruck *et al.* [4] is incorrect. In this section, the GO–PO–PO method is also used in the RCS calculation. It will be shown that the GO method cannot accurately predict the RCS of a self-illuminating corner reflector at boresight unless the dimensions of the corner reflector are extremely large compared to the wavelength. Figs. 4 and 5 show, respectively, the RCS patterns of a square and pentagonal corner reflectors having a panel area of $100\lambda^2/3$ at 9.5 GHz. In these figures, both the GO and GO–PO–PO predictions are shown. It is also shown that the GO solution is overestimating the RCS at boresight and the derivative of the RCS pattern is discontinuous there. The discontinuity of the slope of the RCS pattern (nonphysical) stems from the fact that the illuminated area abruptly changes away from the boresight illumination. The numerical GO–PO–PO solution which include the near-field effects predicts the accurate results, as will be shown in Section III. To make the simple GO solution or self-illuminating corner reflectors useful, the difference between the RCS calculations is predicted by the GO, and GO–PO–PO methods is plotted in Fig. 6 as a function of normalized dimension $\sqrt{A}/\lambda$. Fig. 6 shows that the discrepancy between

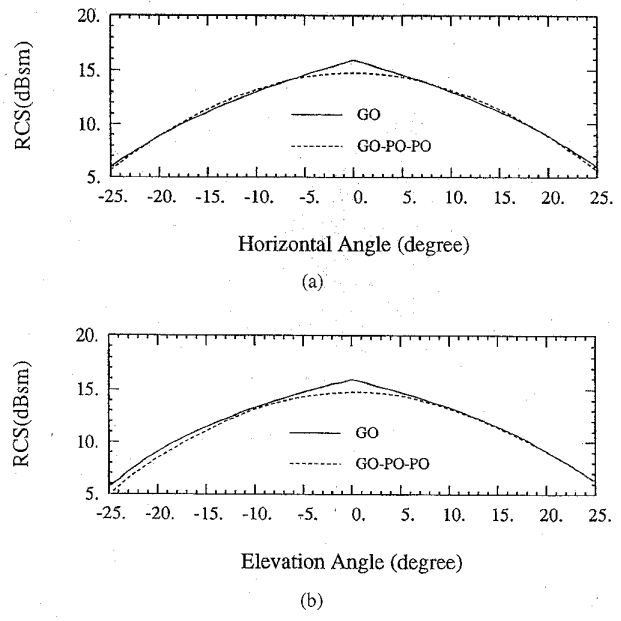

Fig. 4. RCS patterns of a square corner reflector as function of (a) horizontal and (b) elevation angles. Panel area is $100\lambda^2/3$ at 9.5 GHz.

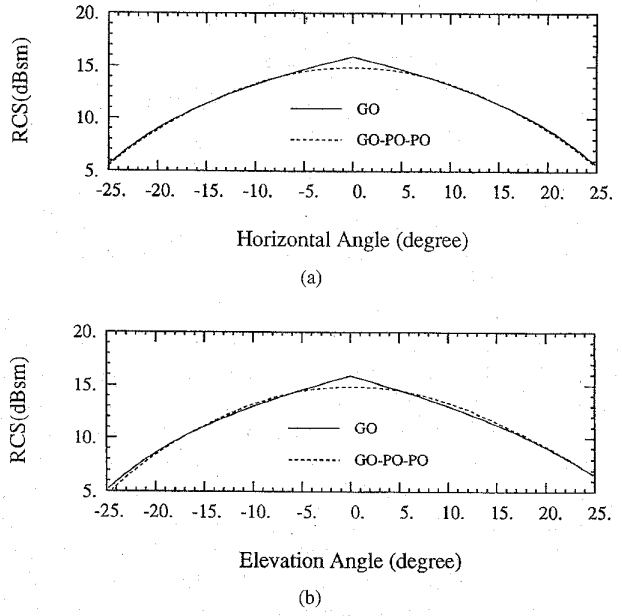

Fig. 5. RCS patterns of a pentagonal corner reflector as function of (a) horizontal and (b) elevation angles. Panel area is $100\lambda^2/3$ at 9.5 GHz.

the GO and GO–PO–PO prediction decreases as $\sqrt{A}/\lambda$ increases.

D. The Self-Illuminating Corner Reflectors

In the previous section, it was shown that every point on the surface of a pentagonal corner reflector contributes to the RCS at boresight. Using the area of the lit region ($A_p = l^2/3$) in (5), the maximum RCS of a pentagonal corner reflector can be obtained from

$$\sigma^p_{\max} = 12\pi \cdot \left(\frac{A_p}{\lambda}\right)^2.$$

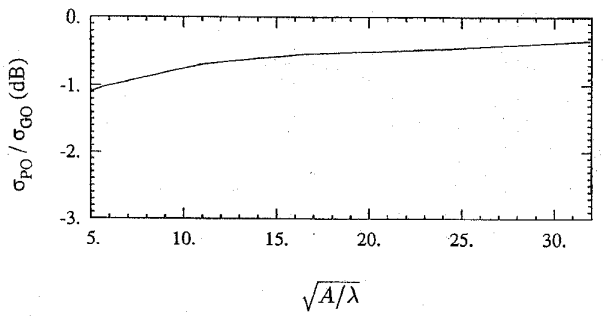

Fig. 6. The ratio of RCS predictions using the GO–PO–PO and GO methods for self-illuminating corner reflectors (square and pentagonal) at boresight illumination.

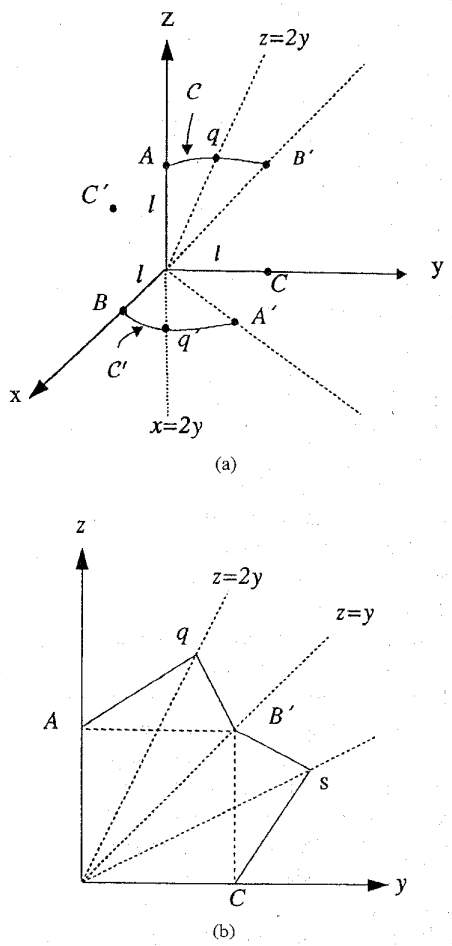

Fig. 7. (a) Mapping of a general curve C from y–z plane to x–y plane after two reflections and (b) the panel geometry of a general self-illuminating hexagonal corner reflector.

However, the maximum RCS for a triangular corner reflector in terms of its panel area A_t is

$$\sigma^t_{\max} = \frac{16\pi}{3} \cdot \left(\frac{A_t}{\lambda}\right)^2$$

which is smaller than that of a pentagonal corner reflector having the same panel area by a factor of 4/9 (−3.5 dB). It was also shown that the lit region (at boresight) after two reflections

has exactly the same geometry as that of the panel (self-illuminated) and, therefore, reflected rays from the ground plane are not captured by the corner reflector cavity. In this section, we seek a class of geometries for the panels of corner reflectors that are self-illuminating at boresight incidence. For these reflectors, every point on the panels will contribute to the backscatter and a maximum RCS of $\sigma_{\max} = 12\pi \cdot (A_p/\lambda)^2$ is achievable independent of panel geometry.

It is required that each panel be illuminated completely at boresight. The self-illuminating requirement imposes a symmetry condition on the acceptable geometries for the panels. That is, the three panels of the corner reflector have to be identical so that the corner reflector becomes self-illuminating at boresight. Suppose the internal edges of a self-illuminating corner reflector coincide with the axes of a Cartesian coordinate system (x, y, z). Let us also denote the tip of each edge along z, x, and y axis by A, B, and C, respectively, as shown in Fig. 7. The incident wave at boresight propagates along

$$\hat{k}_i = -\frac{1}{\sqrt{3}} \cdot \hat{x} - \frac{1}{\sqrt{3}} \cdot \hat{y} - \frac{1}{\sqrt{3}} \cdot \hat{z}.$$

After two reflections, it can be shown that points A, B, and C are imaged on x–y, y–z, and x–z planes which are denoted by A', B', and C', respectively. Representing the internal edge length of the corner reflector by l, coordinates of A', B', and C' are given by $(l, l, 0)$, $(0, l, l)$, and $(l, 0, l)$, respectively. It can also be shown that the region $z \geq y$ in y–z plane is imaged after the first reflection on the first quadrant of x–z plane which in turn is imaged (after the second reflection) on the region $x \geq y$ in x–y plane. Suppose that the boundary of the self-illuminating corner reflector between points A and B' is specified by a curve denoted by $\mathcal{C}$. Considering the symmetry properties of the panel geometry, a similar curve specifies the boundary between points C and B' (mirror image with respect to $z = y$ plane). Therefore, characterization of curve $\mathcal{C}$ would completely specify the geometry of the self-illuminating corner reflector. Assume curve $\mathcal{C}$ is represented by a parametric equation

$$\mathcal{C}(\tau) = [0, f(\tau), g(\tau)], \quad \tau \in [0, t]$$

where the following constraints $f(0) = 0$, $f(t) = l$, $g(0) = l$, and $g(t) = l$ are imposed to ensure that $\mathcal{C}$ would pass through A and B'.

After two reflections, a point p on $\mathcal{C}$ is mapped to p' on x–y plane whose coordinates in terms of p are given by

$$\begin{aligned} x_{p'} &= z_p \\ y_{p'} &= z_p - y_p. \end{aligned} \tag{6}$$

The mapping is a linear transformation which is one-to-one and onto. This transformation maps $\mathcal{C}(\tau)$ to a plane curve $\mathcal{C}'(\tau)$ on x–y lane given by

$$\mathcal{C}'(\tau) = [g(\tau), g(\tau) - f(\tau), 0], \quad \tau \in [0, t].$$

As τ goes from zero to t, $\mathcal{C}$ and $\mathcal{C}'$ trace from A to B' and A' to B, respectively. Noting that the mapped curve in x–y lane must be identical to the curve in y–z plane, there is a parameter $t = t_o$ corresponding to points q and q', so that

$$\begin{aligned} x_{q'} &= z_q \\ y_{q'} &= y_q. \end{aligned} \tag{7}$$

Using (7) in (6), it can be shown that

$$\begin{aligned} z_q &= 2y_q \\ x_{q'} &= 2y_{q'}. \end{aligned}$$

That is, the similar points q and q' on lines $z = 2y$ in y–z plane) and $x = 2y$ (in x–y plane) are reached at the same time. This fact suggests the following procedure for the construction of $\mathcal{C}(\tau)$. Consider an arbitrary point q on the line $z = 2y$ and an arbitrary curve $\mathcal{C}_1(\tau) = [0, f_1(\tau), g_1(\tau)]$ between points A and q. This curve is mapped in x–y plane to

$$\mathcal{C}_1'(\tau) = [g_1(\tau), g_1(\tau) - f_1(\tau), 0], \quad \tau \in [0, t]$$

which spans A' to q'. Since the curve between B' and q ($\mathcal{C}_2$) must be identical to the curve between A' and $q'(\mathcal{C}_1')$, then

$$\mathcal{C}_2(\tau) = [0, g_1(\tau), g_1(\tau) - f_1(\tau)], \quad \tau \in [0, t].$$

The combination of $\mathcal{C}_1$ and $\mathcal{C}_2$ uniquely specify the continuous curve $\mathcal{C}$. It can easily be shown that $\mathcal{C}_2$ is mapped to

$$\mathcal{C}_2'(\tau) = [g_1(\tau), f_1(\tau), 0], \quad \tau \in [0, t]$$

which is identical to $\mathcal{C}_1$ as expected.

Referring to (1) and (2), it can easily be shown that the RCS of all self-illuminating corner reflectors at boresight can be obtained from

$$\sigma_{\max} = 12\pi \cdot \left(\frac{A}{\lambda}\right)^2 \tag{8}$$

where A is the surface area of a panel. An expression for the surface area in terms of the parametric equation of $\mathcal{C}_1$ can be obtained easily and is given by

$$A = 2 \cdot \int_0^t (f_1' g_1 - g_1' f_1)\, d\tau. \tag{9}$$

The geometrical optics expression for RCS given by (8) is valid when all dimensions of the panel are very large compared to the wavelength. As the wavelength increases, contribution from higher order scattering mechanisms, such as edge diffraction, become comparable to GO contribution and, therefore, the accuracy of (8) decreases. Contribution from edge diffraction is proportional to the edge length and, therefore, it is desirable to minimize the length of the corner reflector edges. Moreover, the edge length minimization would minimize the largest dimension of the reflector. The edge length of a self-illuminating corner reflector can be obtained from

$$L = 2 \cdot \int_0^T \left\{ \sqrt{f_1'^2 + g_1'^2} + \sqrt{(f_1' - g_1')^2 + g_1'^2} \right\} d\tau. \tag{10}$$

The optimum corner reflector is a self-illuminating corner reflector whose edge length is minimized. That is, for a given RCS, the optimum corner reflector has the smallest

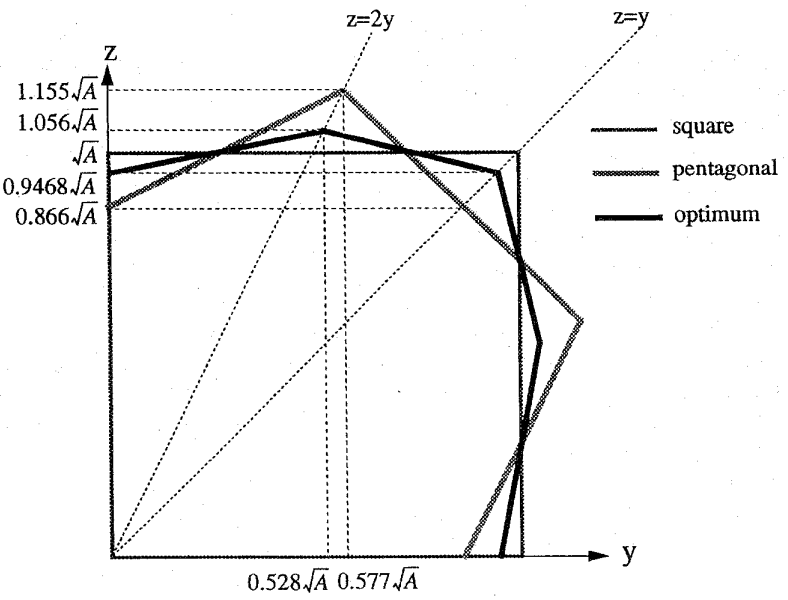

Fig. 8. The geometry of a square, pentagonal, and optimum hexagonal corner reflector having the same panel area.

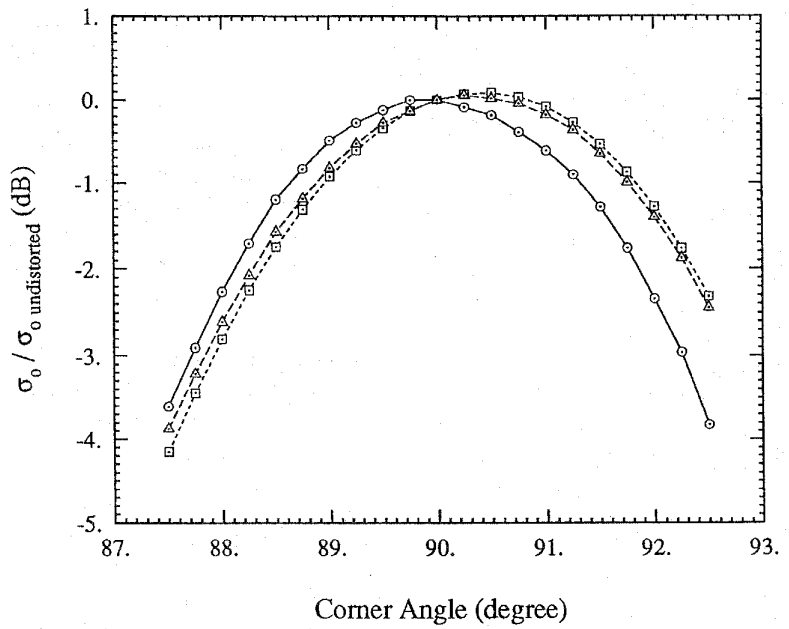

Fig. 9. RCS of distorted corner reflectors normalized to that of the undistorted ones is a function of corner angle. The backscatters are calculated at 9.5 GHz for reflectors with $A_s = A_p = 100\lambda^2/3$ and $A_t = 50\lambda^2$.

surface area and the shortest edge length. Mathematically speaking, $f_1(\tau)$ and $g_1(\tau)$ must be chosen so that they would minimized functional (10) subject to constraint (9). This problem resembles the isoperimetric problem in the variational calculus except for a boundary condition which is not imposed on $f_1(\tau)$ and $g_1(\tau)$. Therefore, the conditions for the fundamental lemma of the calculus of variations [15] are not met and the solution of the isoperimetric problem cannot be used here. Since no analytical procedure can be formulated for the problem at hand, an iterative solution is considered. First, we confine our search to linear functions and obtain an optimum polygonal geometry and use that as an initial guess for the next higher order functions, and so on.

The simplest curve that can be chosen for $\mathcal{C}_1$ is a straight line. Under linear transformation, a line segment is mapped into another line segment and, therefore, the geometry of the panel becomes a general hexagon. This hexagon can easily be generated by choosing an arbitrary point q on $z = 2y$ line, finding its mirror image point with respect to $z = y$ plane (s), and finally connecting points A, q, B', s, and C, as

shown in Fig. 5(b). The square and pentagonal corner reflectors are two special cases of the hexagonal self-illuminating corner reflectors. Basically, points $q_s = (0, l/2, l)$ and $q_p = (0, 2l/3, 4l/3)$ generate a square and a pentagonal corner reflector, respectively. Using (9) and (10) for a linear function, and after a tedious algebraic manipulation, equation of the optimum line describing C_1 is found to be

$$z = 0.2066y + 0.9468\sqrt{A} \tag{11}$$

whereas before, A was the surface area of the panel. The edge length of the optimum hexagonal corner reflector is found to be $1.944\sqrt{A}$ whereas the edge length of the square and pentagonal corner reflectors are $2\sqrt{A}$ and $2.1\sqrt{A}$, respectively. Fig. 8 shows the panel geometry of a square, pentagonal, and the optimum hexagonal corner reflectors having the same surface areas. Higher order curves can be obtained by perturbing (11) which would result in a very complex minimization problem and is not pursued here. The RCS patterns of the square and pentagonal corner reflectors, as shown in Figs. 4 and 5, are very much similar and, therefore, it is expected that the RCS pattern of the optimum corner reflector be similar to those as well.

E. Sensitivity to Corner Angle

One last issue of practical importance is the sensitivity of the corner reflector RCS to deviations of corner angles from 90°. It is quite obvious that any manufacturing error in the corner angle will reduce the nominal RCS value of a corner reflector. In fact, from the GO point of view, the scattered rays after the third reflection are not parallel to the incident ray and, therefore, the RCS predicted by GO for nonperpendicular panels is zero. In reality, the scattered wave from each panel has a finite beamwidth and the PO can be used to predict the RCS. It is reported that the RCS of square corner reflectors are twice as sensitive to errors in the corner angles than that of triangular corner reflectors [3]. In this section, using our GO–PO–PO model, the sensitivity of RCS of triangular and optimal corner reflectors to errors in corner angles is examined. There is more than one way of distorting the corner angles. In this study we modify the corner angles in a symmetrical fashion, that is, increase or decrease all three corner angles simultaneously by the same amount. We also keep the interior edge length of corner reflector constant (same as those of the undistorted ones). Using the GO–PO–PO method, RCS of a triangular, a pentagonal, and a square corner reflector at boresight are computed as a function of the corner angle. Fig. 9 shows the RCS of distorted corner reflectors normalized to that of undistorted ones ($A_t = 50\lambda^2$ or $A_p = A_s = 100\lambda^2/3$ at 9.5 GHz) as a function of the corner angle. It is shown that the sensitivity in corner angle errors for all these corner reflectors is almost on the same order. RCS calculation of metallic plates based on PO approximation is accurate in the mainlobe around the specular direction. Therefore, the accuracy of the GO–PO–PO solution in predicting the RCS of corner reflectors as a function of corner angle deviations is limited to small angles (few degrees from 90°).

III. Experimental Results

In this section, the measured RCS patterns of a triangular, a pentagonal, and a square corner reflector over a wide range of incidence angles at 9.5 GHz are presented and compared with the GO and GO–PO–PO predications. The corner reflectors are designed to have the same geometrical optics RCS of 15.9 dBsm ($A = 332.4$ cm^2). The GO–PO–PO method predicts an RCS of 15.9, 14.8, and 14.7 dBsm for the triangular, square and pentagonal corner reflectors, respectively. Also, the effect of a perfectly conducting ground plane on the RCS is demonstrated experimentally. The backscatter measurements were performed polarimetrically using an HP-8753 network-analyzer-based scatterometer operating in a linear chirped mode. A chirp frequency of 9–10 GHz was used which allowed for a range gating with a spatial resolution of about 15 cm. The measurements were conducted in a 15-m long anechoic chamber where the targets were mounted on a styrofoam pedestal attached to a stepper motor positioner. The effect of the distortion parameters of the radar system, such as the channel imbalances and the antenna cross-talk factors, on the measured scattering matrices were removed using the single target calibration technique (STCT) [14].

Fig. 2 shows the RCS patterns of the triangular corner reflector in the azimuth and elevation planes. Comparison of the measured co-polarized backscatters (σ_{vv}, σ_{hh}) show an excellent agreement with the GO and GO–PO–PO prediction. The measured results indicate a co- to cross-polarized ratio (σ_{vv}/σ_{hv}) of better than 35 dB over the range of incidence angle $-10° < \alpha < +10°$. Similar agreement was obtained for the elevation pattern ($\phi = 45°$). In the elevation plane the cross-polarized RCS remains very low ($\sigma_{vv}/\sigma_{hv} > 35$ dB) over a much wider angular range ($-30° < \theta < +30°$). The 1-dB RCS beamwidths in the horizontal and elevation planes for a triangular corner reflector were found to be 24°. Figs. 10 and 11 show the measured and estimated polarimetric RCS patterns of the square and the pentagonal corner reflectors, in the horizontal and elevation planes. Similar agreement with the GO–PO–PO method was obtained in these two cases. The measured 1-dB RCS beamwidths in the azimuth and elevation planes for the two self-illuminating corner reflector were found to be around 16°.

Next, the effect of the ground plane on the RCS of corner reflectors is examined. First, backscatter cross sections of these three corner reflectors sitting on a large, flat, perfectly conducting ground plane, as shown in Fig. 4(b), were measured. This configuration corresponds to positioning a corner reflector for a SAR at incidence angle ($54.74° - \beta$). Fig. 12 shows the measured RCS of the triangular and pentagonal corner reflectors on the ground plane corresponding to $\beta = 0°$. The measured RCS's are compared with the theoretical RCS predictions of isolated corner reflectors (GO–PO–PO). As mentioned previously the triangular corner reflector can illuminate the ground plane (or receive the reflected ray from the ground plane), hence its RCS is increased whereas the RCS of the self-illuminating reflector is unchanged. For low SAR incidence angles, the lower panel of the reflectors are tilted upward. Fig. 13 shows, respectively, the measured

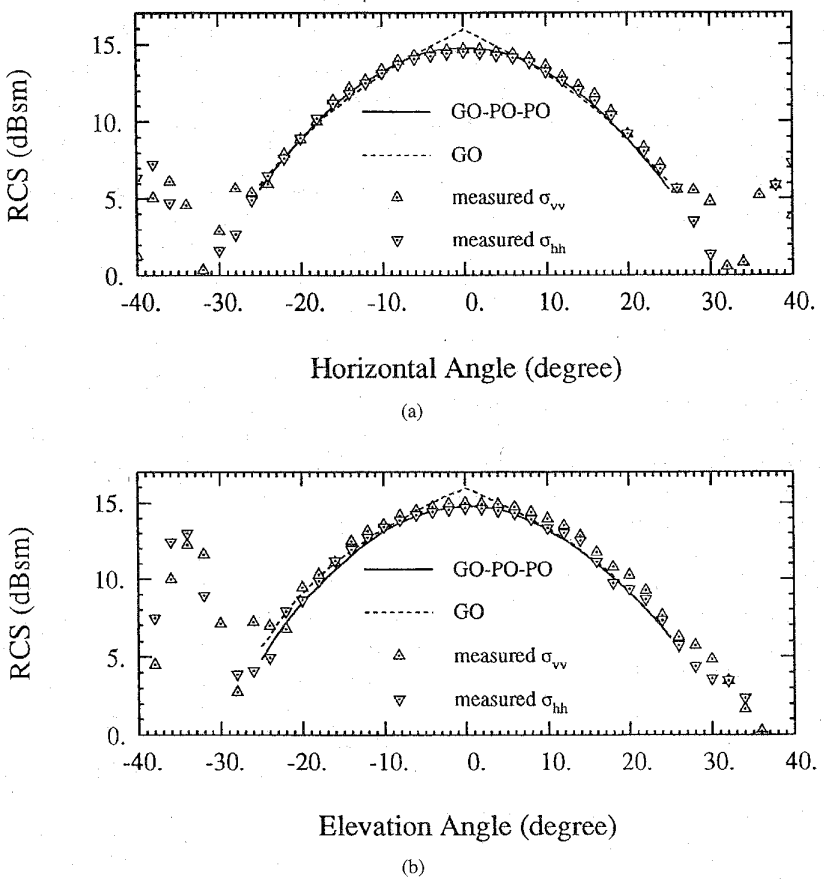

Fig. 10. The measured RCS patterns of a square corner reflector as function of (a) horizontal and (b) elevation angles. Panel area is $100\lambda^2/3$ at 9.5 GHz.

and theoretical RCS of the triangular and pentagonal corner reflectors above the ground plane with $\beta = 10°$. At boresight, the triangular corner reflector shows more serious reduction in RCS while the RCS of the self-illuminating corner reflector is less affected. The reason for such a drastic change in the RCS is the backscatter contribution of the wave which is trapped between the lower panel and the ground plane. This fact was verified experimentally. By placing an absorber under the lower panel, the scattering contribution from the ground plane and the lower panel was suppressed. The RCS of the triangular corner reflector is affected more because of its larger panel size.

The perfectly conducting ground plane enhances the effect of the ground plane on the RCS. In practice corner reflectors are placed above a soil surface. Fig. 14 shows the RCS of the triangular corner reflector and the pentagonal corner reflector above a smooth soil surface with $\beta = 10°$. Again, it can be seen that the RCS of the triangular corner is influenced more drastically than that of the pentagonal corner reflector in the presence of the ground plane.

IV. Conclusion

In this paper, the theoretical and experimental aspects of scattering from corner reflectors are considered. A new class of self-illuminating corner reflectors is introduced which requires the minimum panel area for a given RCS value. The self-illuminating corner reflectors are proposed as calibration targets for imaging radar systems. Also the geometry of the optimum corner reflector which has the shortest edge length among polygonal self-illuminating corner reflectors is obtained. Prototype triangular, pentagonal, and square corner reflectors were constructed and measured at X-band. It was shown that the self-illuminating corner reflectors offer two major improvements over the widely used triangular corner reflectors: 1) the uncertainty in the RCS of self-illuminating corner reflectors, caused by the interaction of the ground plane with the corner reflector, is significantly smaller than that of the triangular corner reflectors and 2) for a specified RCS, the panel area is two-thirds of that of the triangular one. The 1-dB RCS beamwidths of the pentagonal and square corner reflector in azimuth and elevation planes were found to be around 16°.

Appendix A

In this appendix, analytical expressions for the area of the lit region on panel #1 of a triangular corner reflector as a function of azimuth and elevation angles (θ, ϕ) are given. The same expressions can be used to find the area of the lit regions on panels #2 and #3 using the following change of variable

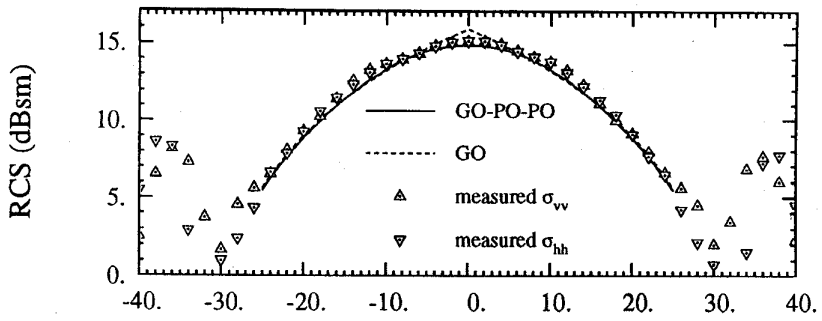

(a)

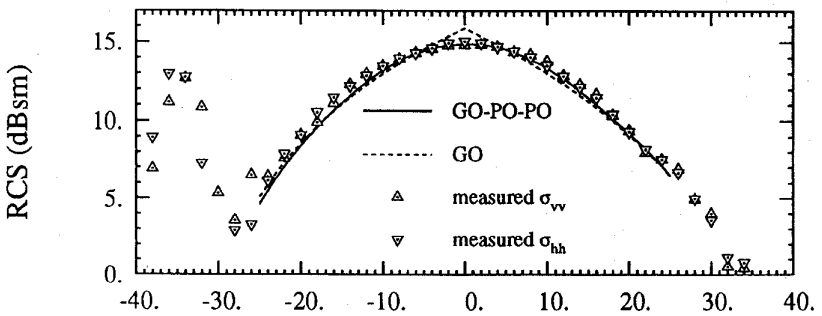

(b)

Fig. 11. The measured RCS patterns of a pentagonal corner reflector as function of (a) horizontal and (b) elevation angles. Panel area is $100\lambda^2/3$ at 9.5 GHz.

for θ and ϕ, respectively

$$\begin{cases} \theta' = & \cos^{-1}(\sin\theta\cos\phi) \\ \phi' = & \tan^{-1}\left(\dfrac{\cos\theta}{\sin\theta\cos\phi}\right) \end{cases}$$

$$\begin{cases} \theta'' = & \cos^{-1}(\sin\theta\sin\phi) \\ \phi'' = & \tan^{-1}\left(\dfrac{\sin\theta\cos\phi}{\cos\theta}\right). \end{cases}$$

Depending on the incidence angles, the lit area for a triangular corner reflector can obtain from equations shown below in which $T_s = \tan\theta\sin\phi$, $T_c = \tan\theta\cos\phi$, $S = \sin\theta$, and $C = \cos\theta$.

- $T_c + T_s \le 1$

$$A_1 = \frac{1}{2}l^2 \cdot T_c T_s \cdot \frac{2 + T_c + T_s}{(1+T_s)(1+T_c)}.$$

- $T_c + T_s > 1$ and $-1 \le T_c - T_s \le 1$

$$A_1 = \frac{1}{2}l^2 \cdot \left\{\frac{T_s - T_c + 1}{T_c + T_s + 1} \cdot \frac{T_c}{1+T_s} + \frac{T_s}{1+T_c} \cdot \frac{T_c - T_s + 1}{T_c + T_s + 1} + \frac{T_c + T_s - 1}{T_c + T_s + 1}\right\}.$$

- $T_c + T_s > 1$ and $T_c - T_s > 1$

$$A_1 = \frac{1}{2}l^2 \cdot \frac{T_s}{1 + T_c + T_s} \cdot \frac{3 + 3T_c - T_s}{1 + T_c}.$$

- $T_c + T_s > 1$ and $T_c - T_s < -1$

$$A_1 = \frac{1}{2}l^2 \cdot \frac{T_c}{1 + T_c + T_s} \cdot \frac{3 + 3T_s - T_c}{1 + T_s}.$$

APPENDIX B

In this appendix (similar to Appendix A), the area of the lit region on panel #1 of a square corner reflector is given.

- $\phi \ge 45^\circ$, $1 \le T_s < 2$, and $T_c \ge 1$

$$A_1 = l^2 \cdot \left(2 - \frac{0.5 \cdot C}{S} - \frac{0.5 \cdot S}{C}\right).$$

- $\phi \ge 45°$, $1 \le T_s < 2$, and $T_c < 1$

$$A_1 = l^2 \cdot \left\{2 \cdot T_c - \frac{0.5 \cdot C}{S} - 0.5 \cdot T_c T_s\right\}.$$

- $45° \le \phi \le \tan^{-1}(2)$, $T_s \ge 2$, and $T_c \ge 1$

$$A_1 = l^2 \cdot \left\{2 - \frac{0.5 \cdot C}{S} - \frac{0.5 \cdot S}{C}\right\}.$$

- $\phi \ge \tan^{-1}(2)$, $T_s \ge 2$, and $T_c \ge 1$.

$$A_1 = \frac{1.5 \cdot l^2 \cdot C}{S}.$$

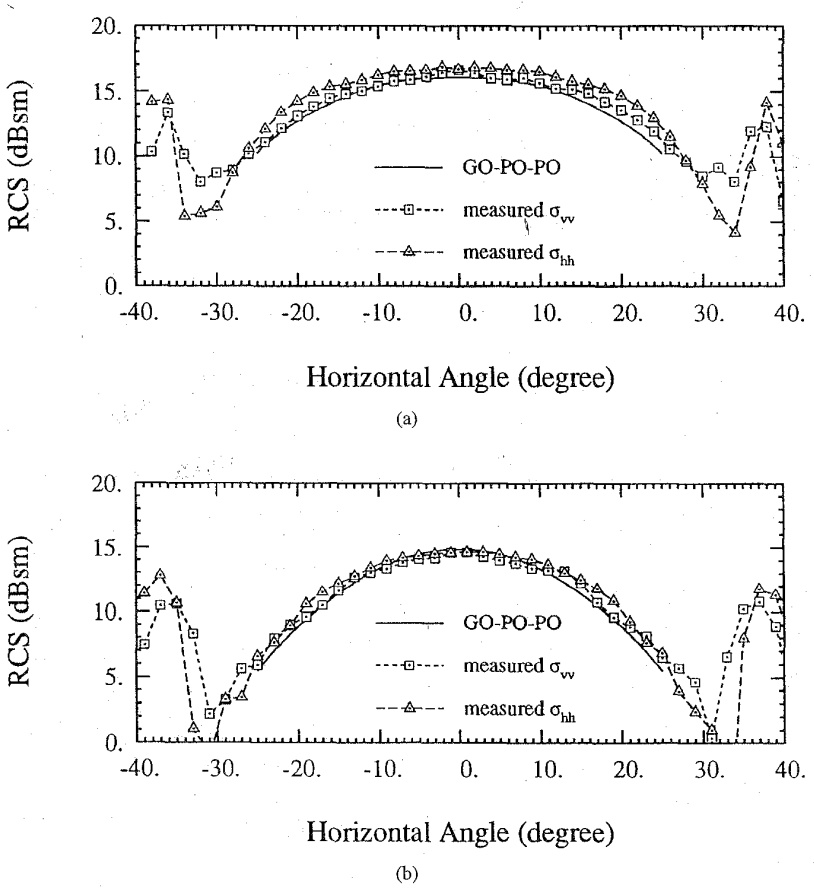

Fig. 12. The measured RCS patterns of: (a) triangular corner reflector with $A_t = 50\lambda^2$ and (b) pentagonal corner reflector with $A_p = 100\lambda^2/3$ at 9.5 GHz above a perfectly conducting ground plane ($\beta = 0°$).

- $\phi \geq 45°$, $T_s \geq 2$, and $T_c < 1$.

$$A_1 = \frac{1.5 \cdot l^2 \cdot C}{S}.$$

- $T_s < 1$, and $T_c < 1$

$$A_1 = l^2 \cdot T_s T_c.$$

- $\phi < 45°$, $1 \leq T_c < 2$, and $T_s < 1$

$$A_1 = l^2 \cdot \left\{ 2 \cdot T_s - \frac{0.5 \cdot S}{C} - 0.5 \cdot T_s T_c \right\}.$$

- $\phi < 45°$, $T_c \geq 2$, and $T_s < 1$

$$A_1 = \frac{1.5 \cdot l^2 \cdot S}{C}.$$

- $\phi < 45°$, $1 \leq T_c < 2$, and $T_s \geq 1$

$$A_1 = l^2 \cdot \left\{ 2 - \frac{0.5 \cdot C}{S} - \frac{0.5 \cdot S}{C} \right\}.$$

- $\tan^{-1}(0.5) \leq \phi < 45° \tan^{-1}(2)$, $T_s \geq 2$, and $T_c \geq 1$

$$A_1 = l^2 \cdot \left\{ 2 - \frac{0.5 \cdot C}{S} - \frac{0.5 \cdot S}{C} \right\}.$$

- $\phi < \tan^{-1}(0.5)$, $T_c \geq 2$, and $T_s \geq 1$

$$A_1 = \frac{1.5 \cdot l^2 \cdot S}{C}.$$

APPENDIX C

In this appendix (similar to Appendix A), the area of the lit region on panel #1 of a pentagonal corner reflector is given. Separate expressions for A_1^{23} and A_1^{32} are derived. The expressions for A_1^{23} are given by

- $T_s < 0.5$, $T_s > 2$, $T_c - T_s > 1$, $T_s - T_c > 2$ or $5T_s - 2T_c < 1$:
  a) $A_1^{23} = 0$. This is an approximation which corresponds to the incidence angles far way from the boresight.
- $\phi < \tan^{-1}(0.5)$;
  a) $2T_c - T_s < 1$

$$A_1^{23} = l^2 \cdot T_c \cdot \frac{5T_s - 1}{12(1 + T_s)}.$$

  b) $1 \leq 2T_c - T_s < 2$

$$A_1^{23} = l^2 \cdot \left\{ \frac{2T_c + T_s - 2}{4(2T_c - T_s + 2)} + T_c \cdot \frac{2 - 2T_c + T_s}{4(2T_c - T_s + 2)} \right\}.$$

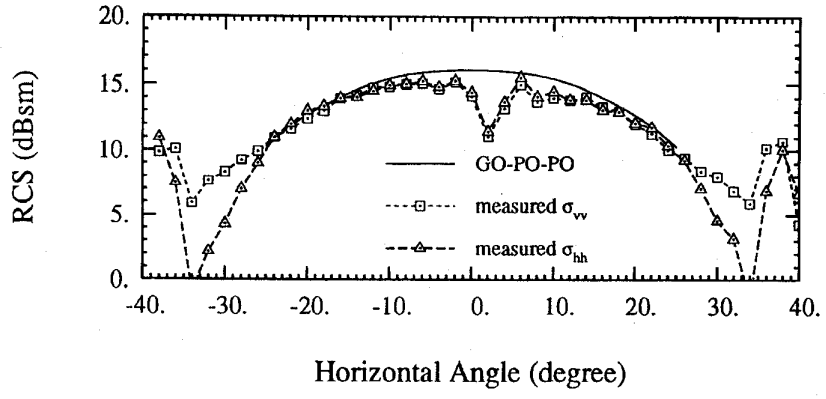

(a)

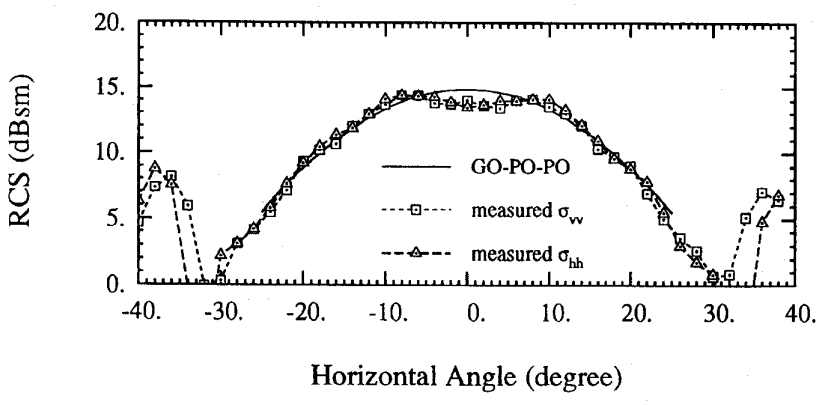

(b)

Fig. 13. The measured RCS patterns of: (a) triangular corner reflector with $A_t = 50\lambda^2$ and (b) pentagonal corner reflector with $A_p = 100\lambda^2/3$ at 9.5 GHz above a perfectly conducting ground plane ($\beta = 10°$).

c) $2T_c - T_s \geq 2$

$$A_1^{23} = l^2 \cdot \frac{T_s}{2(T_s+1)\left(2-\frac{S}{C}\right)}.$$

- $\tan^{-1}(0.5) \leq \phi < \tan^{-1}(2)$:

a) $T_c + T_s \leq 2,\ 2T_c - T_s < 1$

$$A_1^{23} = l^2 \cdot T_c \cdot \frac{5T_s - 1}{12(1+T_s)}.$$

b) $T_s + T_c \leq 2,\ 2T_c - T_s \geq 1$

$$A_1^{23} = l^2 \cdot \left\{ \frac{2T_c + T_s - 2}{4(2T_c - T_s + 2)} + T_c \cdot \frac{2 - 2T_c + T_s}{4(2T_c - T_s + 2)} \right\}.$$

c) $T_s + T_c > 2,\ 2T_c - T_s < 1$

$$A_1^{23} = l^2 \cdot \left\{ T_c \cdot \frac{T_s - T_c + 1}{T_s + 1} \cdot \frac{1}{2(T_c + T_s + 1)} + \frac{T_c + T_s - 1}{2\left(\frac{S}{C}+1\right)(T_c + T_s + 1)} \right\}.$$

d) $T_s + T_c > 2,\ 2T_c - T_s < 1 \geq 1$

$$A_1^{23} = l^2 \cdot \frac{5S - C}{12(C+S)}.$$

- $\phi \geq \tan^{-1}(2)$:

a) $2T_s - T_c < 2$

$$A_1^{23} = l^2 \cdot T_c \cdot \frac{5T_s - 1}{12(1+T_s)}.$$

b) $2 \leq 2T_s - T_c < 2.5,\ T_s + T_c < 2$

$$A_1^{23} = l^2 \cdot T_c \left\{ \frac{2T_s - 1}{12(1+T_s)} + \frac{2T_c - 4T_s + 5}{6(4 + T_c - 2T_s)} + \frac{\frac{1-2}{2S-C}}{2(4 + T_c - 2T_s)} \right\}.$$

c) $2 \leq 2T_s - T_c < 2.5,\ T_s + T_c \geq 2$

$$A_1^{23} = l^2 \cdot \left\{ \frac{T_c}{2(T_s+1)(T_s + T_c + 1)} + \frac{2(T_s + T_c) - 1}{6(T_s + T_c + 1)} + \frac{S - 2C}{6(2S - C)} \right\}.$$

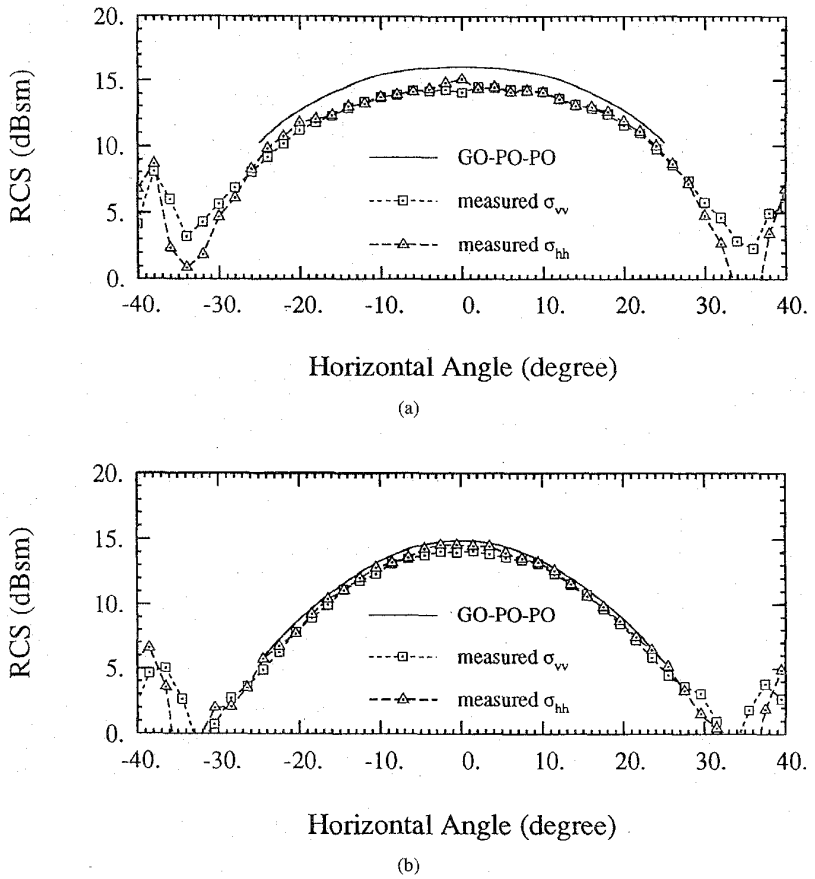

Fig. 14. The measured RCS patterns of: (a) triangular corner reflector with $A_t = 50\lambda^2$ and (b) pentagonal corner reflector with $A_p = 100\lambda^2/3$ at 9.5 GHz above a lossy dielectric ground plane ($\beta = 10°$).

d) $2T_s - T_c \geq 2.5,\ T_s - 2T_c > 0.5$

$$A_1^{23} = l^2 \cdot \left\{ T_c \cdot \frac{T_s + T_c + 1}{2(T_s+1)(2T_s - T_c + 2)} + \frac{|2T_s - T_c + 2 - 1|}{\left(\frac{2S}{C} - 1\right)(2T_s - T_c + 2)} \right\}.$$

e) $2T_s - T_c \geq 2.5,\ T_s - 2T_c \leq 0.5$

$$A_1^{23} = l^2 \cdot \left\{ \frac{T_c}{2(T_s+1)(T_s+T_c+1)} + \frac{2(T_s+T_c)-1}{6(T_s+T+1)} + \frac{S-2C}{6(2S-1C)} \right\}.$$

The expressions for A_1^{32} are given by

- $T_c < 0.5,\ T_c > 2,\ T_s - T_c > 1,\ T_c - T_s > 2$ or $5T_c - 2T_s < 1$:

  a)

  $$A_1^{32} = 0.$$

  This is an approximation which corresponds to the incidence angles far way from the boresight.

- $\phi < \tan^{-1}(0.5)$:

  a) $2T_c - T_s < 2$

  $$A_1^{32} = l^2 \cdot T_s \cdot \frac{5T_c - 1}{12(1+T_c)}.$$

  b) $2 \leq 2T_c - T_s < 2.5,\ T_s + T_c < 2$

  $$A_1^{32} = l^2 \cdot \left\{ T_s \cdot \frac{2T_c - 1}{6(1+T_c)} + \frac{2T_s + 3}{6(4 + T_s - 2T_c)} + \frac{\frac{T_s+2}{\left(\frac{2C}{S} - 1\right)}}{2(4 + T_s - 2T_c)} \right\}.$$

  c) $2 \leq 2T_c - T_s < 2.5,\ T_s + T_c \geq 2$

  $$A_1^{32} = l^2 \cdot \left\{ \frac{C - 2S}{6(2C - S)} + \frac{|5T_s - T_c - 1|}{6(T_s + T_c + 1)} + \frac{T_s(T_c - T_s + 1)}{2(T_c+1)(2T_c - T_s + 1)} \right\}.$$

d) $2T_c - T_s \geq 2.5,\ T_s + T_c < 0.5$

$$A_1^{32} = l^2 \cdot \left\{ \frac{S|T_c(3C-S)-(T_c+1)|}{2C(2C-S)(2T_c-T_s+2)} + \frac{T_s(T_c+T_s+1)}{2(T_c+1)(2T_c-T_s+2)} \right\}.$$

e) $2T_s - T_c \geq 2.5,\ T_s + T_c \geq 2$

$$A_1^{32} = l^2 \cdot \left\{ \frac{C-2S}{6(2C-S)} + \frac{|5T_s-T_c-1|}{6(T_c+T_s+1)} + \frac{T_s(T_c-T_s+1)}{2(T_c+1)(T_c+T_s+1)} \right\}.$$

- $\tan^{-1}(0.5) \leq \phi < \tan^{-1}(2)$:

a) $T_c + T_s \leq 2,\ 2T_s - T_c < 1$

$$A_1^{23} = l^2 \cdot T_s \cdot \frac{5T_c-1}{12(1+T_c)}.$$

b) $T_s + T_c \leq 2,\ 2T_s - T_c \geq 1$

$$A_1^{23} = l^2 \cdot \left\{ \frac{2T_s+T_c-2}{4(2T_s-T_c+2)} + T_s \cdot \frac{2-2T_s+T_c}{4(2T_s-T_c+2)} \right\}.$$

c) $T_s + T_c > 2,\ 2T_s - T_c < 1$

$$A_1^{23} = l^2 \cdot \left\{ T_s \cdot \frac{T_c-T_s+1}{T_c+1} \cdot \frac{1}{2(T_c+T_s+1)} + \frac{T_c+T_s-1}{2\left(\frac{C}{S}+1\right)(T_c+T_s+1)} \right\}.$$

d) $T_s + T_c > 2,\ 2T_s - T_c < 1 \geq 1$

$$A_1^{23} = l^2 \cdot \frac{5C-S}{12(C+S)}.$$

- $\phi < \tan^{-1}(2)$:

a) $2T_s - T_c < 1,$

$$A_1^{23} = l^2 \cdot T_s \cdot \frac{5T_c-1}{12(1+T_c)}.$$

b) $1 \leq 2T_s - T_c < 2$

$$A_1^{32} = l^2 \cdot T_s \cdot \left\{ \frac{2-2T_s+T_c}{2(2T_s-T_c+2)} + \frac{2T_s+T_c-2}{2(T_c+1)(2T_s-T_c+2)} \right\}.$$

c) $2T_s - T_c \geq 2$

$$A_1^{32} = l^2 \cdot \frac{C}{4(2S-C)}.$$

REFERENCES

[1] K. Sarabandi, L. E. Pierce, and F. T. Ulaby, "Calibration of a polarimetric imaging SAR," *IEEE Trans. Geosci. Remote Sensing,* vol. 30, no. 3, pp. 540–549, May 1992.

[2] J. J. van Zyl, "Calibration of polarimetric radar images using only image parameters and trihedral corner reflector responses," *IEEE Trans. Geosci. Remote Sensing,* vol. 28, no. 3, pp. 337–348, May 1990.

[3] R. C. Spencer, "Optical theory of the corner reflectors," MIT, Cambridge, MA, Radiation Lab. Rep. 433, Mar. 1944.

[4] G. T. Ruck, *Radar Cross Section Handbook.*. New York: Plenum Press, 1970, pp. 588–597.

[5] L. N. Ridenour, *Radar System Engineering*. New York: McGraw-Hill, 1946, pp. 67–68.

[6] L. Peters, Jr., "Passive bistatic radar enhancement devices," *IEE Proc.,* vol. 109, pt. C, no. 15, pp. 1–10, Mar. 1962.

[7] D. R. Sheen, A. Freeman, and E. S. Kasischke, "Phase calibration of polarimetric SAR images," *IEEE Trans. Geosci. Remote Sensing,* vol. 27, no. 6, pp. 719–731, Nov. 1989.

[8] K. Sarabandi, L. E. Pierce, Y. Oh, M. C. Dobson, F. T. Ulaby, A. Freeman, and P. Dubois, "Cross-calibration experiment of JPL AIRSAR and truck-mounted polarimetric scatterometer," *IEEE Trans. Geosci. Remote Sensing,* vol. 32, no. 5, pp. 975–985, Sept. 1994.

[9] T. Griesser and C. A. Balanis, "Backscatter analysis of dihedral corner reflectors using physical optics and the physical theory of diffraction," *IEEE Trans. Antennas Propagat.,* vol. 35, no. 10, pp. 1137–1147, Oct. 1987.

[10] T. B. A. Senior and K. Sarabandi, "Scattering models for point targets," in *Radar Polarimetry for Geosci. Applications,* F. T. Ulaby and C. Elachi, Eds. Dedham, MA: Artech House, 1990, ch. 3, p. 61.

[11] S. D. Robertson, "Targets for microwave radar navigation," *Bell Syst. Tech. J.,* vol. 26, pp. 852–869, 1947.

[12] E. F. Knott, *Radar Cross Section Measurements.*. New York: Van Nostrand Reinhold, 1993, p. 188.

[13] C. T. Tai, "Some essential formulas in dyadic analysis and their applications," *Radio Sci.,* vol. 22, no. 7, pp. 1283–1288, Dec. 1987.

[14] K. Sarabandi and F. T. Ulaby, "A convenient technique for polarimetric calibration of single-antenna radar systems," *IEEE Trans. Geosci. Remote Sensing,* vol. 28, no. 6, pp. 1022–1033, Nov. 1990.

[15] J. D. Logan, "Calculus of variation," in *Applied Mathematics—A Contemporary Approach.* New York: Wiley, 1987, ch. 3, pp. 84–150.

Kamal Sarabandi (S'87–M'90–SM'93) for photograph and biography, see p. 266 of the February 1996 issue of this TRANSACTIONS.

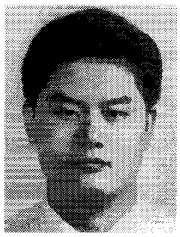

Tsen-Chieh Chiu was born in Kaohsiung, Taiwan, on November 3, 1968. He received the B.S. and M.S. degrees in electrical engineering from National Taiwan University, Taipei, Taiwan, in 1990 and 1992, respectively. He is currently working toward the Ph.D. degree in electrical engineering at the University of Michigan, Ann Arbor

He is currently a Research Assistant with the Radiation Laboratory, University of Michigan, Ann Arbor. His research interests include microwave remote sensing and calibration of the radar system.